Showcasing research from laboratories of Professor Choi, School of Science, Xi'an Jiaotong-Liverpool University, Suzhou, China, Professor Cho, Department of Materials Science & Engineering, Ajou University, Suwon, Korea, and Dr. Ko, Korea Institute of Ceramic Technology, Jinju, Korea.

Overcoming the limitations of atomic-scale simulations on semiconductor catalysis with changing Fermi level and surface treatment

A new method of density functional theory calculation introduced in this article allows accurate predictions of surface reactions on wide band gap semiconductors in atomic-scale without limitations of cell size, which was not possible with conventional density functional theory calculations.

As featured in:

See Hyunseok Ko, Sung Beom Cho, Heechae Choi *et al.*, *J. Mater. Chem. A*, 2024, **12**, 33537.

ROYAL SOCIETY OF CHEMISTRY

rsc.li/materials-a

Registered charity number: 207890

Journal of Materials Chemistry A

ROYAL SOCIETY OF CHEMISTRY

PAPER

View Article Online
View Journal | View Issue

Cite this: J. Mater. Chem. A, 2024, 12, 33537

Overcoming the limitations of atomic-scale simulations on semiconductor catalysis with changing Fermi level and surface treatment†

Seulgi Ji,[a] Dong Won Jeon,[bc] Junghyun Choi,[d] Haneol Cho,[e] Bo-In Park,[f] Ilpyo Roh,[g] Hyungil Choi,[g] Chansoo Kim,[el] Jung Kyu Kim,[h] Uk Sim,[i] Danlei Li,[j] Hyunseok Ko,*[k] Sung Beom Cho *[bc] and Heechae Choi *[aj]

Received 23rd May 2024
Accepted 21st August 2024

DOI: 10.1039/d4ta03595j

rsc.li/materials-a

Wide band gap metal oxide semiconductor catalysts mostly exhibit very huge variations of catalytic reaction activities and pathways depending on the preparation conditions, unlike metallic catalyst materials. Atomic-scale modeling and *ab initio* calculations are extremely challenging for metal oxide semiconductor catalysts because of two main reasons: (i) large discrepancies between computational predictions and experiments, (ii) typical cell size limitations in modeling for dilute level doping (<10^{20} cm^{-3}) cocatalyst size-dependency (diameter >3 nm). In this study, as a new groundbreaking methodology, we used a combination of density functional theory (DFT) calculations and a newly derived analytical model to systematically investigate the mechanisms of catalytic methane (CH_4) oxidation activity change of CeO_2. The key hypothesis that the catalytic methane oxidation reaction can be followed by the Fermi level change in CeO_2 was well demonstrated *via* comparison with our multi-scale simulation and several literature reports. Our new method was found to give predictions in the catalytic activity of wide band gap semiconductors for variations in defect concentrations and cocatalyst coverage with advanced efficiency and accuracy, overcoming the typical model size limitation and inaccuracy problems of DFT calculations.

Introduction

To boost and optimize the methane (CH_4) oxidation reaction catalyzed by CeO_2-based catalysts in solid oxide fuel cell (SOFC) anodes, a number of materials engineering strategies and mechanism studies have been performed.[1] As the most widely used routes to improve the catalytic activity of CeO_2 in methane oxidation, cocatalyst deposition and impurity doping methods have been intensively used.[2–4] Atomic scale modeling based computational studies have been performed along with experiments to understand how the catalytic methane oxidation activities of CeO_2 are highly enhanced by up to several orders even with only very low cocatalyst coverage *via* cocatalyst nanoparticle (NP) deposition and/or dilute-limit impurity doping.[5–7] However, it is extremely challenging to investigate the mechanism by experiments and density functional theory calculation based analysis on wide band gap CeO_2 (ref. 6) because the catalytic activity of CeO_2 catalysts greatly varies with the deposited NP size and the doping concentration.[8–11]

In previous theoretical studies, the dopant sites on the CeO_2 surface or the cocatalyst surfaces were commonly regarded as the main active sites due to the significantly increased catalytic activities.[12–14] For example, in theoretical studies on silver- and copper-doped CeO_2 systems, surface-doping was assumed in the catalytic reaction modeling.[15,16] However, experimental

[a]Institute of Inorganic Chemistry, University of Cologne, Greinstr. 6, Cologne, 50939, Germany. E-mail: heechae.choi@xjtlu.edu.cn
[b]Department of Materials Science and Engineering, Ajou University, Suwon, 16499, Republic of Korea. E-mail: csb@ajou.ac.kr
[c]Department of Energy Systems Research, Ajou University, Suwon, 16499, Republic of Korea
[d]School of Chemical, Biological and Battery Engineering, Gachon University, Seongnam-si, Gyeonggi-do 13120, Republic of Korea
[e]AI, Information and Reasoning (AI/R) Laboratory, Korea Institute of Science and Technology (KIST), Hwrangro 14Gil 5, Seoul, Republic of Korea
[f]Department of Mechanical Engineering, Massachusetts Institute of Technology, Cambridge, MA, USA
[g]MO R&D Center, M.O.P Co., Ltd, Seoul, 07281, Republic of Korea
[h]School of Chemical Engineering, Sungkyunkwan University (SKKU), Suwon, 16419, Republic of Korea
[i]Hydrogen Energy Technology Laboratory, Korea Institute of Energy Technology (KENTECH), Naju, 58330, Republic of Korea
[j]Department of Chemistry, Xi'an Jiaotong-Liverpool University, Suzhou, 215123, China
[k]Center of Material Digitalization, Korea Institute of Ceramic Engineering and Technology (KICET), Jinju, Gyeongnam, 52851, Republic of Korea. E-mail: hko@kicet.re.kr
[l]AI-Robot Department, University of Science and Technology (UST), Republic of Korea

† Electronic supplementary information (ESI) available. See DOI: https://doi.org/10.1039/d4ta03595j

studies proved that the intrinsic n-type characteristic of CeO_2 was even enhanced with Ag- and Cu-doping, as the dopants are mostly segregated in the CeO_2 grain boundaries.[17,18] Therefore, it is a more appropriate assumption that the doped metal impurities in CeO_2 do not participate in the surface reaction directly, as demonstrated by several previous experimental studies;[19,20] the main roles of metal element doping in CeO_2 are not the formation of new kinds of active sites.

For the NP-decorated CeO_2 catalyst case, the synergistic effects in the methane oxidation of metallic Ni/CeO_2 heterojunctions were explained using adsorption energy calculations and the Mars–Van Krevelen (MvK) mechanism at the interface.[21,22] However, the assumption that the main contributions to catalytic reactions are made by the active sites of cocatalyst NPs deposited on CeO_2 cannot support mechanism analysis for many other cases. For example, the catalytic CH_4 reactivity of cocatalyst deposited CeO_2 peaks only with very low coverage of cocatalysts.[23] Furthermore, some research revealed that the dominant surface orientations,[24] morphology,[12,25,26] terminations,[22] or the atomic percentages of cocatalyst NP elements on CeO_2 largely determine the catalytic activity of metal NP decorated CeO_2.[27,28] Such findings contradictory to the conventional assumptions in the modeling schemes imply that the cocatalyst deposition and impurity doping contribute to the changed activity of the CeO_2 surface in different ways which were never discussed. To advance the rational engineering of the wide band gap CeO_2 catalyst, further mechanism study is necessary.

In most of the previous experimental and computational studies, the possibility that the surface electronic structure of CeO_2 is tuned by cocatalyst NPs and dopants was hardly considered even though only low coverage of NPs improves the catalytic activity of CeO_2 in methane oxidation.[2,23,29] Recent semiconductor photochemistry studies revealed that the surface activities of wide band gap oxide materials can be tuned *via* surface Fermi level modifications with metal deposition or dopant segregation.[30–32] An experimental and computational study on the nickel nitride decorated CeO_2 catalyst reported that the electron transferred from the cocatalyst to the CeO_2 support affects the catalytic activity of CeO_2.[33]

In recent experimental and computational research works on wide band gap oxide materials, we demonstrated that catalytic reactions on the oxide surface were greatly altered *via* manipulation of the Fermi level either by doping or surface treatment,[34,35] whereas the importance of the Fermi level in the catalytic reactions of CeO_2 has never been discussed. Heterovalent dopants in CeO_2 or point defects can change the bulk Fermi level due to the changed charge carrier concentration and accordingly band bending occurs near the surface because the bulk Fermi level ($\varepsilon_{F(bulk)}$) and surface Fermi level (ε_F) deviate from each other (Fig. 1).[36,37] Therefore, the surface Fermi level can be modulated by the difference between $\varepsilon_{F(bulk)}$ and the degree of band bending (ΔV_{BB}) (eqn (1)); when cocatalyst NPs are loaded on the CeO_2 surface, the surface Fermi level can be directly altered by the energy band alignment with the work function of the decorated cocatalyst NPs ($\varnothing_{cocat}$) at the equilibrium state as shown in Fig. 1.[38]

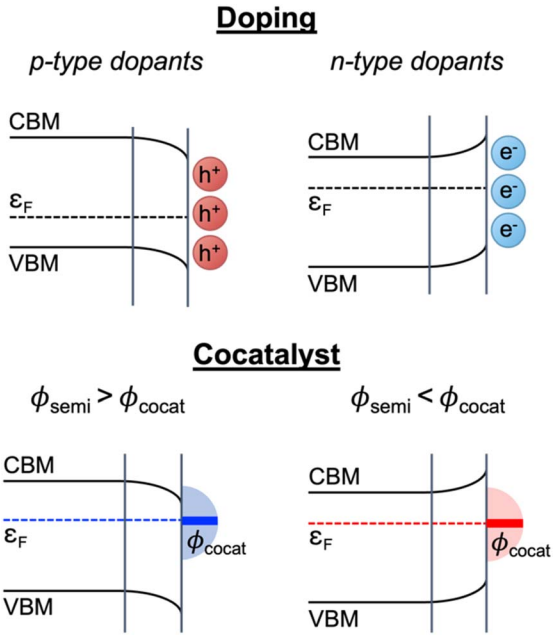

Fig. 1 Schematic illustration of surface Fermi level modification strategies: doping and cocatalyst.

$$\varepsilon_F = \varepsilon_{F(bulk)} - \Delta V_{BB} \quad (1)$$

According to the theoretical model described above, a variation of the surface Fermi level of a semiconductor determines the favorable charge states of adsorbed species and the adsorption energies. Since an electron transfer between a semiconductor surface and the highest occupied molecular orbital (HOMO) or lowest unoccupied molecular orbital (LUMO) of adsorbates contributes to the Gibbs free energy change by chemisorption, the Fermi level of a semiconductor catalyst must be taken into account for an adsorption energy calculation (Fig. 1).[39,40] In our recent previous theoretical–experimental combinational works, we introduced a new theoretical method for better understanding of the relationships between the surface Fermi level and the adsorption energy on wide band gap semiconductors.[34,35,41] We successfully controlled the surface reaction kinetics by manipulating the surface Fermi level and theoretically elucidated the influence of surface Fermi level engineering on the adsorption energy.

In this study, we investigate the mechanism of methane oxidation and the promoting effect of doping/cocatalyst decoration on the catalytic activity of CeO_2 with a key hypothesis: catalytic methane oxidation reaction activity of the CeO_2 catalyst is determined by the surface Fermi level. By using DFT calculations and our new analytical models, we proved that the catalytic methane oxidation reactions on CeO_2 are highly dependent on the surface Fermi level. In comparison to our new theoretical predictions with many experimental studies in the literature, the dopant–cocatalyst synergies and cocatalyst coverage effects were successfully explained.

Results and discussion

Theory

As a method to resolve the inevitable discrepancy between the charge transfer energetics of a semiconductor in real life and the DFT electronic structure predictions (Fig. 2), we express the adsorption energy of adsorbates on a semiconductor as a function of the Fermi level. In the conventional method, the Gibbs free energies of adsorbates on catalytic surfaces have been calculated by using the computational hydrogen electrode (CHE) model proposed by Norskov *et al.*[42] In this work, a Gibbs free adsorption energy (ΔG_{ads}) of a methane oxidation intermediate adsorbate on a CeO_2 surface was expressed as

$$\Delta G_{ads} = \Delta E_0 + q(\varepsilon_F + E_{VBM}) + E_{iso} - E_{per} + q\Delta V + \Delta ZPE + \int C_p dT - T\Delta S \quad (2)$$

where ΔE_0 is the binding energy of adsorbates on CeO_2. q, ε_F and E_{VBM} in eqn (2) are the charge states of the adsorbates, the Fermi level that ranged over the bandgap of CeO_2 (111), and the DFT-computed eigenvalue of the VBM energy level of the CeO_2 (111) slab with the adsorbate, respectively.[34,35,41] For the correction of the formation energies of finite-size supercells with charged defects, we added slab-based correction terms, E_{iso}, E_{per} and $q\Delta V$, which are the self-interaction of the isolated charge distribution and the energy of the model charge embedded in the model dielectric medium under periodic boundary conditions, respectively. ΔV is the difference between the potential of the model charge system and DFT calculations. The terms ΔZPE, $\int C_p dT$ and ΔS in eqn (2) are the changes of zero-point energy, enthalpic, and entropy contributions at temperature T to the Gibbs free energy of an adsorbate, respectively. A detailed description of the computational method and discussion regarding the terms in eqn (2), the charge state of adsorbates, and the adsorption energy graphs are given in sections 1, 2, and 3 of the ESI and Fig. S1,† respectively.

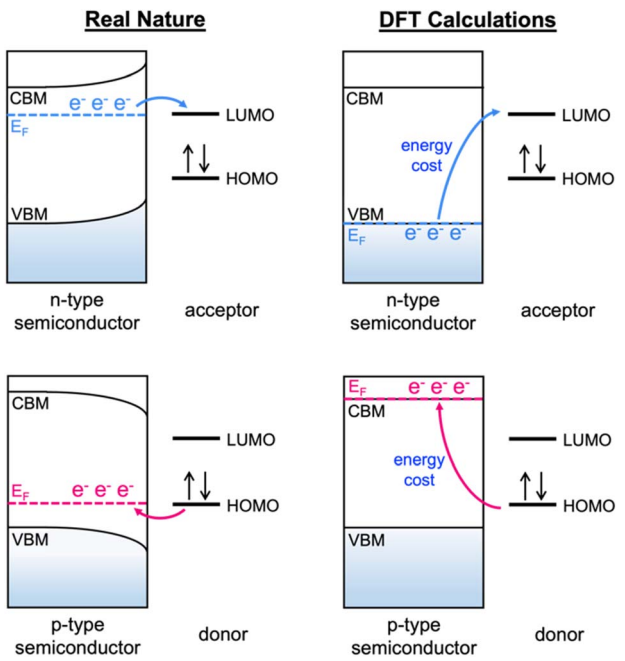

Fig. 2 A schematic illustration of the inevitable error of adsorption energy between real life and DFT calculations.

Fermi level dependent reaction pathway and energy barrier

In Fig. 3, we present how the surface Fermi level of CeO_2 can alter the methane oxidation reaction pathway and change the reaction energy barrier. We considered the methane oxidation reaction at 923 K (650 °C), a typical reaction temperature of SOFC, in the reaction intermediate free energy calculations.[43] Concerning the adsorption of a CH_4 molecule on a CeO_2 (111) for an initiation of the CH_4 oxidation reaction, the positive value of the adsorption energy (2.75 eV) of a CH_4 molecule on a CeO_2 (111) surface (*CH_4 formation) is not energetically favored, as shown in Fig. S1.† On the other hand, the calculated adsorption free energies in Fig. S2† show that negatively charged *O (*O^{2-}) can significantly occupy the active sites of CeO_2 when the Fermi level of CeO_2 is above 1.58 eV, as the adsorption free energy becomes negative and competes with the adsorbate of reaction step 1 (*CH_3 formation). Therefore, the methane oxidation reactant oxygen reservoir is O_2(g) (*O^{2-}) with the Fermi level below (above) 1.58 eV. The descriptions of reaction steps, reaction pathways, and the optimized configurations of adsorbates are presented in Scheme S1, ESI 4, and Fig. S3.†

The free energy diagrams of the methane oxidation reactions catalyzed by neutral (ε_F = 1.6 eV), extreme p-type (ε_F = 0.3 eV), and n-type (ε_F = 2.9 eV) CeO_2 with the thermodynamically preferred intermediates and the atomic structure of each reaction step are presented in Fig. 3a and b to examine whether the Fermi level can affect the reaction pathway and energy barriers. The detailed free energy diagrams of methane oxidation on CeO_2 with all possible intermediates are depicted in Fig. S4†. All the excessive charges in the models were localized on intermediates on the CeO_2 surface. (Fig. S5†) We additionally calculated the density of states (DOS) of each intermediate (CH_3, CH_2, CH, and CHO), which can be charged during methane oxidation, to see the effect on the change to the electronic states of CeO_2. Fig. S6† shows that the adsorption of the charged CH_2 and CH resulted in the formation of gap states, while there is no gap state formation by CH_3 and CHO adsorption. According to the calculated free energy diagram in Fig. 3a, CH_2 and CH are expected not to bind residually to the CeO_2 surface for so long but to form CHO, showing the free energy downhill in reaction step 4. Therefore, we reason that the change to the surface Fermi level position due to the generated gap state by CH_2 and CH adsorption can be negligible.

The charge state of *CH_3 in reaction step 1 is positive (CH_3^+) on the p-type (ε_F = 0.3 eV) and the neutral (ε_F = 1.6 eV) CeO_2, and turns negative (CH_3^-) on the n-type (ε_F = 2.9 eV) CeO_2. Since the adsorbed *O^{2-} is stabilized on the n-type CeO_2 surface due to the stronger binding to the surface Ce ion, the formation of *CH_3^- is suppressed. According to the calculated energy diagram in Fig. 3a, dehydrogenation reactions are all energy downhill from the reaction steps 1 to 4, regardless of the surface Fermi level position of CeO_2. Our theoretical prediction of

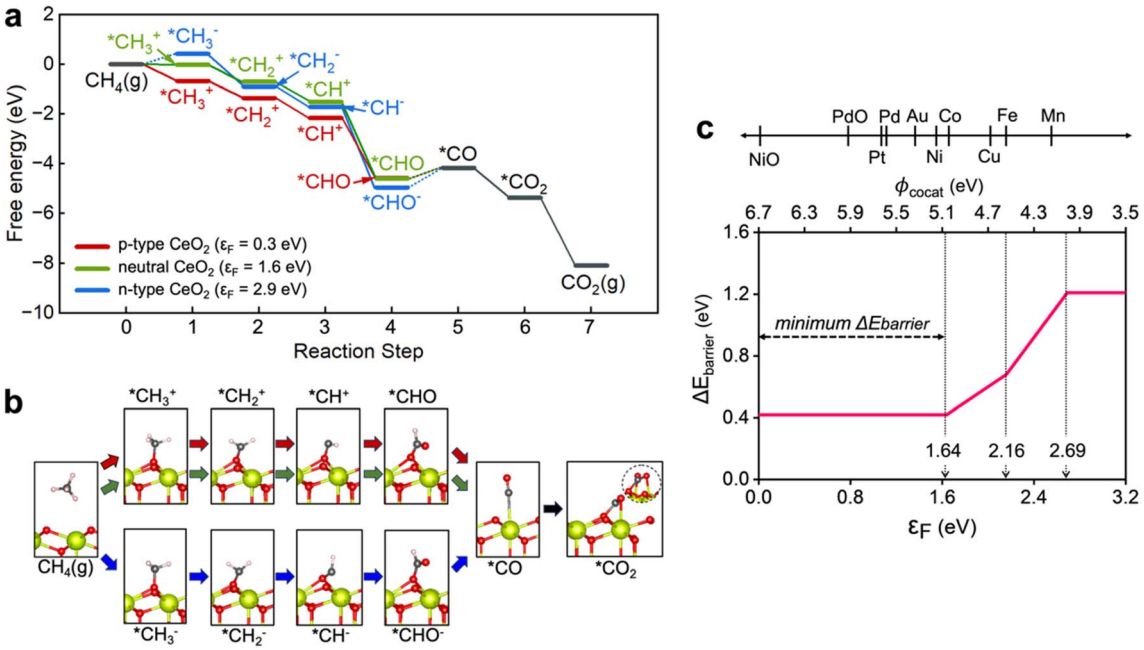

Fig. 3 DFT calculations of methane oxidation on a CeO_2 (111) surface with Fermi level variation: (a) calculated free energy diagrams and (b) the atomic structures of the methane oxidation reaction pathways on the p-type ($\varepsilon_F = 0.3$ eV), neutral ($\varepsilon_F = 1.6$ eV), and n-type ($\varepsilon_F = 2.9$ eV) CeO_2. (c) Total energy barrier as a function of the Fermi level of CeO_2 and cocatalyst work function. Black lines in (a) indicate the energy levels in the reaction steps 5–7 in the methane oxidation, which are the same regardless of the Fermi level of CeO_2. Solid and dashed lines in (a) indicate the energy downhill and uphill reactions, respectively.

energy downhills for reaction steps 1 to 4 is well consistent with the experimental *in situ* observations in the CeO_2 catalyst that the CH_2 group was not detected due to the too short lifetime.[21] For reaction step 4 in Fig. 3a, our calculations predicted that *C adsorption on CeO_2 was not thermodynamically stable (Fig. S3†). Instead, *CHO formation is expected to be favored with neutral charge ($q = 0$) on the p-type CeO_2 and negative charge ($q = -1$) on the n-type CeO_2. Since the adsorption energy of $*CHO^-$ becomes more negative with the higher Fermi level of CeO_2, the energy uphill becomes larger with the CeO_2 surface Fermi level. The formation of the $*CHO^-$ adsorbate on CeO_2 catalyst surfaces during methane oxidation reactions is consistent with the experimental observations of significant stretching vibration frequencies of CHO^- groups at 1735, 1715, and 1704 cm^{-1}.[44,45]

General methods to control the surface Fermi level of wide band gap semiconductors include (i) impurity doping,[46] (ii) grain size control,[47] and (iii) deposition of other NPs on the surface.[48] However, it is extremely challenging to lower the Fermi level of CeO_2 *via* impurity doping or grain size control because even metal dopants having a smaller valence preserve the intrinsic n-type characteristic of CeO_2, as the dopants are segregated at grain boundaries,[17,18] and the size effects on surface band bending can be valid only when the grain radius is smaller than the charge depletion region width (<30 nm).[47] However, most of the CeO_2 catalysts have grain size greater than 50 nm.[12,28,49] Therefore, surface NP deposition is the only available methods. To give a quantitative insight, the total energy barrier, the summation of the energy barriers of the endothermic reaction steps for methane oxidation on CeO_2 (Fig. S7†), was plotted with respect to the surface Fermi level of CeO_2 (ε_F) as shown in Fig. 3c.

To enhance the reactivity of methane oxidation on CeO_2, the Fermi level of CeO_2 should be controlled in the following ways: (i) hindering the strong adsorption of the O atom, so that $*CH_3$ can dominantly occupy the active site of CeO_2 and (ii) the total energy barrier including two endothermic reaction steps for $*CH_3$ and *CO formation should be minimized. The adsorption free energy diagram at where the Fermi level is in a range between 0 eV and 1.64 eV is depicted in Fig. S8†. Our theoretical prediction that cocatalysts have work functions between 5.06 eV and 6.70 eV is consistent with many experimental findings such as for CeO_2 decorated with Ni,[21,26,28] Pt,[50,51] Pd,[1,12,52] and Au.[22]

When a cocatalyst is placed on a semiconductor surface, due to the work function difference, a quadratic change in the surface Fermi level on the semiconductor side is induced by band bending. Then, accordingly, the reaction energy barriers and the resultant reaction rate are also changed with the radial distance from the interface between the cocatalyst NP and the semiconductor as the total energy barrier of methane oxidation is assumed to have linearity with the Fermi level (Fig. 3c). Hence, in order to make an accurate prediction of the overall reaction rate, it is necessary to utilize analytical models integrating the changes in the reaction rates with distance from the cocatalyst.

Analytical models for the combinatorial effect of cocatalyst dispersion and work function

We built the analytical model for precise prediction of the reaction rates for methane oxidation catalyzed by cocatalyst-

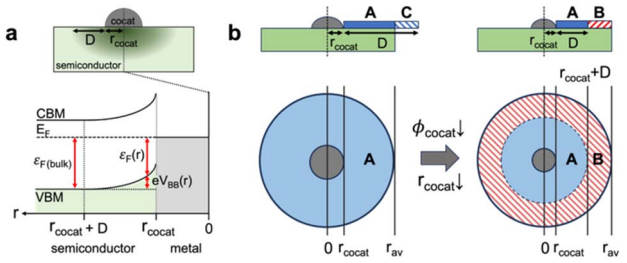

Fig. 4 A schematic illustration of the analytical model for prediction in the catalytic reactivity of CeO_2: (a) a scheme of the calculation model of the cocatalyst-loaded CeO_2 to calculate the surface reaction rate; (b) two cases of depletion region formation on the CeO_2 surface. The blue color area is the depletion region (band bending area, *A*), and the red color area is the area where cocatalyst loading does not affect the Fermi level.

decorated CeO_2 as shown in Fig. 4. Given that the work functions of the predicted cocatalyst candidates are larger than that of CeO_2, we considered Schottky contact between a cocatalyst NP and CeO_2 (Fig. 4a). In the cocatalyst–CeO_2 junction, the surface Fermi level ($\varepsilon_F(r)$) and the degree of band bending ($V_{BB}(r)$) vary with the distance from the loaded cocatalyst (r), which is presented as eqn (3) below,

$$\varepsilon_F(r) = \varepsilon_{F(CeO_2)} - eV_{BB}(r) \quad (3)$$

With considerations of the Fermi-level-dependent adsorption energy model and the change in the reaction rate with distance from the cocatalysts (r), we can assume that the band bending is induced near the cocatalyst/CeO_2 interface in a radial direction from the center of a cocatalyst.[36] In general, the cocatalyst NPs with a diameter of 1–10 nm are deposited on a CeO_2 surface;[48] we employed a model of hemispherical cocatalyst NPs on a semiconductor surface to consider the Fermi level change by the band bending near the interface of cocatalyst NPs and CeO_2. The band bending induced by the work function difference between a cocatalyst and CeO_2 can be expressed using the Poisson equation in the three-dimensional form in a spherical coordinate as

$$V_{BB}(r) = \frac{eN_d}{\varepsilon_r\varepsilon_0}\left[\frac{(D + r_{cocat})^2}{2} - \frac{r^2}{6} - \frac{(D + r_{cocat})^3}{3r}\right] \quad (4)$$

where N_d, ε_r, ε_0, D, and r_{cocat} in eqn (4) are the space charge density, the relative dielectric constant of CeO_2, which is 23,[53] the vacuum permittivity (8.854×10^{-12} C V^{-1} m^{-1}),[54] the width of the depletion region, and the radius of a loaded cocatalyst, respectively. Using the fixed value of r to r_{cocat}, we can obtain the width of the depletion region (D) by using eqn (5)

$$V_{BB}(r_{cocat}) = \phi_{cocat} - \phi_S = \frac{eN_d}{\varepsilon_r\varepsilon_0}\left[\frac{(D + r_{cocat})^2}{2} - \frac{r_{cocat}^2}{6} - \frac{(D + r_{cocat})^3}{3r_{cocat}}\right] \quad (5)$$

The equation of reaction rate constant (R) can be employed to compare the surface reaction activity of cocatalyst/CeO_2 and bare CeO_2 for methane oxidation, which can be written as[55]

$$R = A\exp\left(-\frac{\Delta E_{barrier}}{kT}\right) \quad (6)$$

where A in eqn (6) is the frequency factor, *i.e.*, the number of attempts to react by vibrations, and $\Delta E_{barrier}$ is related to the total energy barrier that we calculated above in Fig. 3c, respectively. To compare the reaction rate with/without cocatalysts on CeO_2, we expressed the surface reaction rate constant ratio (R_1/R_0) where R_1 and R_0 are the surface reaction rate constants of methane oxidation on CeO_2 with/without cocatalyst at the induced band bending area (dark green-color area in Fig. 4a) as follows

$$\frac{R_1}{R_0} = \gamma\int_{r_{cocat}}^{r_{cocat}+D}\frac{\theta_{ads}{}^1}{\theta_{ads}^0}\exp\left(\frac{\Delta E_{barrier}^0 - \Delta E_{barrier}{}^1}{kT}\right)2\pi r dr \quad (7)$$

where θ_{ads} in eqn (7) is the coverage of adsorbates. The graph of coverage of $*CH_3$ (θ_{*CH_3}) and *O (θ_{*O}) considering the competing reaction between $*CH_3$ and *O in the first reaction step is depicted in Fig. S9†.

Given that the functionality and selectivity of catalysts are governed by the coverage and dispersion of a cocatalyst on a semiconductor,[56,57] the effect of cocatalyst coverage and dispersion on the reaction rate was considered by adding the γ term in eqn (7), which is the ratio of the active site on the CeO_2 surface and can be represented by eqn (8),

$$\gamma = 1 - \frac{r_{cocat}{}^2\pi}{A_{semi}} \quad (8)$$

where A_{semi} can be rewritten as $r_{av}{}^2\pi$ and r_{av} is half of the average distance between adjacent cocatalysts. The detailed derivation of the surface reaction rate constant ratio in eqn (7) is described in ESI 5.†

Fig. 4b shows two cases of depletion region formation on a cocatalyst-loaded CeO_2 surface. If the band bending occurs at a wider area in the depletion region than half of the average distance between cocatalysts, the band bending area (blue color area *A* in Fig. 4b) can be distributed in all areas of the exposed CeO_2 surface, where the reaction ratio can be obtained using eqn (7) above. On the other hand, with a decrease in the work function and/or radius of a cocatalyst, band bending occurs at a narrower area than half of the average distance between cocatalysts; therefore, a flat band area (red-hatched area *B* in Fig. 4b) can exist on the CeO_2 surface. The ratio of reaction rate constant on the flat band area ranging from $r_{cocat+D}$ to r_{av} can be calculated by using eqn (7).

In previous studies, without the assumptions of the band bending dependency of the methane oxidation reaction on CeO_2, cocatalyst coverage effects were not fully understood.[36,58] The reaction rate of methane oxidation in the band bending area is approximately 9 times higher than that of the flat band area of CeO_2 for $N_d = 10^{19}$ cm^{-3} (Fig. 4b and S10†). This indicates that the considerations of cocatalyst dispersion (coverage) are a crucial factor due to the changed band bending and Fermi level positions with radial distance from a cocatalyst.

Hence, the contour maps of the surface reaction rate constant ratio (R_1/R_0) as a function of the cocatalyst work function and the active sites ratio (γ) were calculated using eqn (9) and (10):

(i) $r_{cocat} + D$ is narrower than r_{av},

$$\frac{R_1}{R_0} = \gamma\left[\int_{r_{cocat}}^{r_{cocat}+D} \frac{\theta_{ads}{}^{1}}{\theta_{ads}^{0}} \exp\left(\frac{\Delta E_{barrier}^{0} - \Delta E_{barrier}{}^{1}}{kT}\right) 2\pi r dr + \int_{r_{cocat}+D}^{r_{av}} \frac{\theta_{ads}{}^{1}}{\theta_{ads}^{0}} \exp\left(\frac{\Delta E_{barrier}^{0} - \Delta E_{barrier}{}^{1}}{kT}\right) 2\pi r dr\right] \quad (9)$$

(ii) $r_{cocat} + D$ is wider than r_{av},

$$\frac{R_1}{R_0} = \gamma\int_{r_{cocat}}^{r_{av}} \frac{\theta_{ads}{}^{1}}{\theta_{ads}^{0}} \exp\left(\frac{\Delta E_{barrier}^{0} - \Delta E_{barrier}{}^{1}}{kT}\right) 2\pi r dr \quad (10)$$

Optimum cocatalyst coverage and space charge density predictions

In most experimental studies on cocatalyst-deposited CeO_2 catalysts, the methane oxidation reaction activities are sensitively changed with the combination of many factors, such as cocatalyst species, dispersion distance, size, and impurity concentrations in CeO_2 supports.[8] To further verify our hypothesis of the Fermi level dependent methane oxidation reaction rate of the CeO_2 catalyst, we plotted the ratio of the reaction rate by the use of a cocatalyst (R_1/R_0), with contour maps for the simultaneous variations of cocatalyst work function, coverage, and the nonstoichiometry of CeO_2 in Fig. 5 using eqn (9) and (10). The areas enclosed by the dashed curves in Fig. 5 indicate the optimum cocatalyst deposition conditions for high catalytic activity of methane oxidation. For a high coverage of cocatalysts (lower γ value) with high work function for $N_d = 10^{19}$ cm^{-3} a lower reaction rate was shown than that with a low coverage of cocatalysts (higher γ value). A number of previous experimental and theoretical studies have reported that the high coverage of a cocatalyst on CeO_2 can lower the catalytic reaction.[2,6,23,29] For example, Lustemberg *et al.* reported that an undoped CeO_2 catalyst particle with low NiO coverage of 0.10–0.13 ML induces the highest reaction rate of methane oxidation, which is in good accordance with our theoretical observation in Fig. 5 for $N_d = 10^{19}$ cm^{-3} (dashed circle at $0.87 < \gamma < 0.93$).[6] Considering the interface between the loaded catalyst and CeO_2 as the only area where the reaction dominantly takes place, Ni and NiO on CeO_2 were predicted to have a total energy barrier of 0.41 eV for the whole methane oxidation (Fig. 3c). However, with our analytical model, we can reason that the different interface band bending of the Ni/CeO_2 and the NiO/CeO_2 systems will result in different overall reaction activity over the CeO_2 active site area.

The effects of oxidation of metal cocatalysts on the activity of the methane oxidation reaction catalyzed by a CeO_2 catalyst have not been actively discussed before. Pd^0 and Ni^0 species deposited on the CeO_2 catalyst surface are commonly oxidized and behave as the main active species in experimental studies.[1,12,21,59] The methane oxidation reaction activity on the CeO_2 catalyst is rather improved when the Pd and Ni particles are oxidized to form PdO and NiO.[12,59,60] The enhanced methane oxidation reaction activity of the CeO_2 catalyst by cocatalyst oxidation in the literature[12,59,60] agrees very well with our theoretical predictions in Fig. 5: the higher reaction rate ratio of PdO/CeO_2 (work function 6.00 eV) than that of Pd/CeO_2 (work function 5.60 eV) and Pt/CeO_2 (work function 5.65 eV). Considering that the work function of bimetallic catalysts has a linear trend with different compositions of bimetallic alloys,[61] bimetallic cocatalysts with CeO_2 can also be used by manipulation of metal composition to change the work function and thus the depletion region width[62–65] such as in the case of the CuNi/CeO_2 catalyst reported by Hornes *et al.*[14]

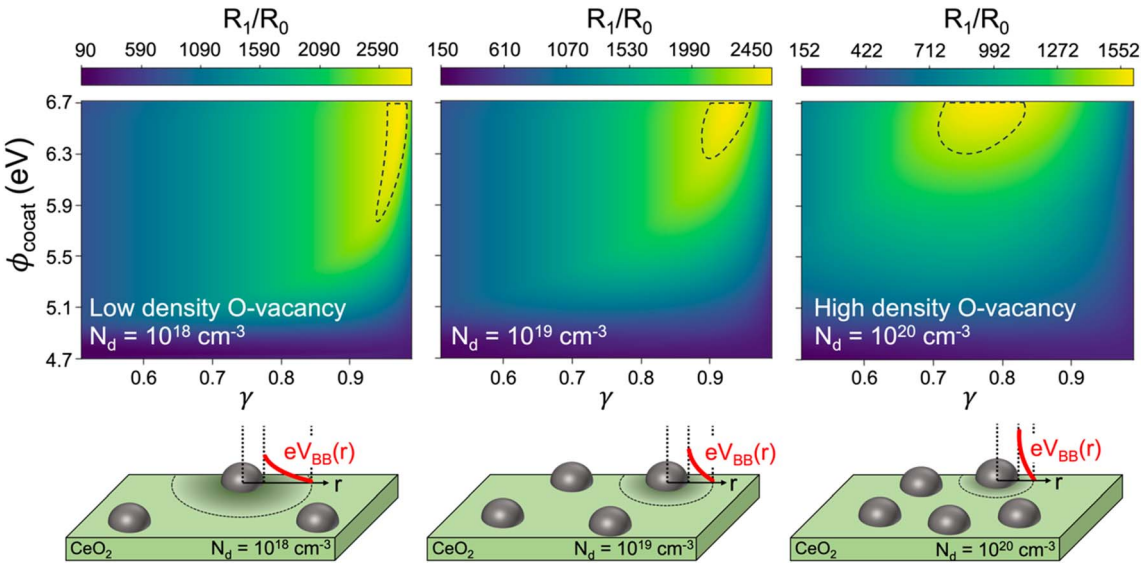

Fig. 5 Top: The contour map of the surface reaction rate ratio (R_1/R_0) of a cocatalyst/CeO_2 (R_1) to that of bulk CeO_2 without a cocatalyst (R_0) as a function of cocatalyst work function (φ_{cocat}) and the ratio of active sites (γ) with various space charge density (N_d) values. The areas enclosed by the dashed curves represent the reaction conditions for the high reactivity of methane oxidation. Bottom: Schematic illustration of the relation between N_d and the cocatalyst dispersion on CeO_2 by the changed band bending potential change at the interfaces (V_{BB}).

Many research studies have already been devoted to studying the effect of oxygen vacancy formation in CeO_2 on the oxidation reaction.[4,5] Due to the unique properties of the Ce^{4+}/Ce^{3+} redox pair of CeO_2, the oxidation reaction on cocatalyst-decorated CeO_2 has been explained by the MvK mechanism, in which lattice oxygen atoms of CeO_2 are involved in the oxidation reaction.[21,22,66,67] However, the underlying reaction mechanisms and active site are still controversial because the optimum cocatalyst coverage differs with the species of cocatalyst, especially when Ce^{3+} species have high concentrations.[12,21]

The first few cycles of methane oxidation on CeO_2 can dominantly follow the MvK mechanism. However, as the methane oxidation takes place continuously, the oxygen vacancy formation energy increases.[68,69] Accordingly, the contribution of the MvK mechanism to the methane oxidation, where oxygen vacancy formation is involved, is rapidly decreased as the Fermi level increases. Therefore, it is insufficient to explain the long-term oxidation reaction by the MvK mechanism alone. To precisely predict the reaction conditions of CeO_2 for even long-term methane oxidation, the synergistic effect of the formation of oxygen vacancies and the change in band bending with increasing the surface Fermi level of CeO_2 on the reaction rate should be considered.

As the oxygen vacancy formation shifts the Fermi level of CeO_2 higher, the surface band bending is induced at the narrower area in the depletion region width (eqn (5) and Fig. S11†). Sm^{3+}, Eu^{3+}, or Zr^{4+} doping in Ni/CeO_2 increases electron concentration (higher N_d value) by segregation at the grain boundary and oxygen vacancy formation. Ni NPs cluster more densely in a few nanometers than in the depletion region width, resulting in the high cocatalyst coverage (lower γ value).[4,5,7] On the other hand, the distribution of dispersed Ni NPs of undoped Ni/CeO_2 is wider (higher γ value) than that of heterovalent dopant doped CeO_2,[4] which is consistent with our calculations. Thus, our theoretical model can provide further elucidation on the oxidation reaction on CeO_2, considering oxygen vacancy formation can change the Fermi level to heavy n-type CeO_2, allowing us to understand the mechanism, including the long-term catalytic reaction.

Conclusions

As a new breakthrough method to solve the problem of inaccurate adsorption energy calculations and the model size limitation problem in the conventional DFT calculations for optimizing wide band gap semiconductor catalysts, we introduced a combination of Fermi level dependent adsorption energy theory and analytical models. In this work, methane oxidation on CeO_2 (with a band gap of 3.2 eV) was used as the case model. Our DFT calculation results showed that the surface Fermi level position of the CeO_2 catalyst can alter the reaction energy barrier and also the reaction pathways, which can clearly explain why only a few specific cocatalyst elements, such as Ni, Pt, Pd, and Au, are used in most of the literature. The combination of the DFT calculations and a new analytical model was used to consider the band bending effects at the cocatalyst–CeO_2 interface to accurately predict the relation between the methane oxidation reactivity of CeO_2 and the cocatalyst coverage. In addition, the synergistic effects of CeO_2-doping concentration and cocatalyst deposition conditions in the methane oxidation reaction activity were successfully explained. The newly suggested method of this work is expected to be widely used for efficient optimization of doping concentration (bulk Fermi level position) and cocatalyst materials, without suffering from the typical cell size limitation problems in atomic-scale modeling for DFT calculations on modified wide band gap semiconductor catalysts.

Data availability

The data supporting this article have been included as part of the ESI.†

Author contributions

Conceptualization, methodology, software, writing – original draft: S. Ji, H. Ko, S. B. Cho, H. Choi. Supervision, writing – review & editing: D. Li, J. K. Kim, U. Sim, H. Ko, S. B. Cho, H. Choi. Formal analysis: H. Cho, C. Kim. Data curation, visualization: S. Ji, D. W. Jeon, H. Cho, C. Kim. Investigation: S. Ji, J. Choi, B.-I. Park, I. Roh, H. Choi.

Conflicts of interest

There are no conflicts to declare.

Acknowledgements

This research was supported by the National R&D Program through the National Research Foundation of Korea (NRF) funded by the Ministry of Science and ICT (RS-2023-00209910, RS-2023-00285390, RS-2024-00444182 and RS-2024-00407282) and Virtual Engineering Platform Project through the Ministry of Trade, Industry, and Energy of Korea (P0022336). We acknowledge the grant no. 2021-0-02076 and 2023-00262155 (IITP) funded by the Korea government (the Ministry of Science and ICT). D. Li is thankful for the support through the Research Development Fund by Xi'an Jiaotong-Liverpool University. H. Choi acknowledges the financial support received through an Enhancement Fund (AY23/24) from the School of Science at Xi'an Jiaotong-Liverpool University. We acknowledge and are thankful for the support received from the Suzhou Industrial Park High Quality Innovation Platform of Functional Molecular Materials and Devices (YZCXPT2023105) and the XJTLU Advanced Materials Research Center (AMRC).

Notes and references

1 J. Lee, T. H. Lim, E. Lee and D. H. Kim, *ChemCatChem*, 2021, **13**, 3706–3712.
2 Y. Lykhach, S. M. Kozlov, T. Skála, A. Tovt, V. Stetsovych, N. Tsud, F. Dvořák, V. Johánek, A. Neitzel, J. Mysliveček, S. Fabris, V. Matolín, K. M. Neyman and J. Libuda, *Nat. Mater.*, 2016, **15**, 284–288.

3 J. Dou, Y. Tang, L. Nie, C. M. Andolina, X. Zhang, S. House, Y. Li, J. Yang and F. Feng Tao, *Catal. Today*, 2018, **311**, 48–55.
4 J. Chen, B. D. Carlson, T. J. Toops, Z. Li, M. J. Lance, S. G. Karakalos, J.-S. Choi and E. A. Kyriakidou, *ChemCatChem*, 2020, **12**, 5558–5568.
5 L. M. Toscani, M. S. Bellora, C. Huck-Iriart, A. L. Soldati, J. Sacanell, T. S. Martins, A. F. Craievich, M. C. A. Fantini, S. A. Larrondo and D. G. Lamas, *Appl. Catal., A*, 2021, **626**, 118357.
6 P. G. Lustemberg, Z. Mao, A. Salcedo, B. Irigoyen, M. V. Ganduglia-Pirovano and C. T. Campbell, *ACS Catal.*, 2021, **11**, 10604–10613.
7 Z. Zhang, Z. Yu, K. Feng and B. Yan, *Appl. Catal., B*, 2022, **317**, 121800.
8 A. Ruiz Puigdollers, P. Schlexer, S. Tosoni and G. Pacchioni, *ACS Catal.*, 2017, **7**, 6493–6513.
9 M. Sterrer, M. Yulikov, E. Fischbach, M. Heyde, H.-P. Rust, G. Pacchioni, T. Risse and H.-J. Freund, *Angew. Chem., Int. Ed.*, 2006, **45**, 2630–2632.
10 S. Abbet, A. Sanchez, U. Heiz, W.-D. Schneider, A. M. Ferrari, G. Pacchioni and N. Rösch, *J. Am. Chem. Soc.*, 2000, **122**, 3453–3457.
11 H. Wang, X.-K. Gu, X. Zheng, H. Pan, J. Zhu, S. Chen, L. Cao, W.-X. Li and J. Lu, *Sci. Adv.*, 2019, **5**, eaat6413.
12 S. Chen, S. Li, R. You, Z. Guo, F. Wang, G. Li, W. Yuan, B. Zhu, Y. Gao, Z. Zhang, H. Yang and Y. Wang, *ACS Catal.*, 2021, **11**, 5666–5677.
13 Y. Mahara, J. Ohyama, T. Tojo, K. Murata, H. Ishikawa and A. Satsuma, *Catal. Sci. Technol.*, 2016, **6**, 4773–4776.
14 A. Hornés, P. Bera, M. Fernández-García, A. Guerrero-Ruiz and A. Martínez-Arias, *Appl. Catal., B*, 2012, **111–112**, 96–105.
15 G. Righi, R. Magri and A. Selloni, *J. Phys. Chem. C*, 2020, **124**, 17578–17585.
16 K. Polychronopoulou, A. A. AlKhoori, A. M. Efstathiou, M. A. Jaoude, C. M. Damaskinos, M. A. Baker, A. Almutawa, D. H. Anjum, M. A. Vasiliades, A. Belabbes, L. F. Vega, A. F. Zedan and S. J. Hinder, *ACS Appl. Mater. Interfaces*, 2021, **13**, 22391–22415.
17 M. Arshad, A. Iqbal, T. Ahamad, J. Gupta, M. Arshad and A. S. Ahmed, *J. Electron. Mater.*, 2023, **52**, 5690–5706.
18 P. Knauth and H. L. Tuller, *Solid State Ionics*, 2000, **136–137**, 1215–1224.
19 F. Khojasteh, M. R. Mersagh and H. Hashemipour, *J. Alloys Compd.*, 2022, **890**, 161709.
20 N. W. Kwak, S. J. Jeong, H. G. Seo, S. Lee, Y. Kim, J. K. Kim, P. Byeon, S.-Y. Chung and W. Jung, *Nat. Commun.*, 2018, **9**, 4829.
21 J. Chen, T. Buchanan, E. A. Walker, T. J. Toops, Z. Li, P. Kunal and E. A. Kyriakidou, *ACS Catal.*, 2021, **11**, 9345–9354.
22 H. Ha, S. Yoon, K. An and H. Y. Kim, *ACS Catal.*, 2018, **8**, 11491–11501.
23 P. Pal, R. K. Singha, A. Saha, R. Bal and A. B. Panda, *J. Phys. Chem. C*, 2015, **119**, 13610–13618.
24 G. B. Hoflund, Z. Li, T. J. Campbell, W. S. Epling and H. W. Hahn, *MRS Online Proc. Libr.*, 1999, **581**, 449.
25 G. Spezzati, A. D. Benavidez, A. T. DeLaRiva, Y. Su, J. P. Hofmann, S. Asahina, E. J. Olivier, J. H. Neethling, J. T. Miller, A. K. Datye and E. J. M. Hensen, *Appl. Catal., B*, 2019, **243**, 36–46.
26 J. Chen, H. N. Pham, T. Mon, T. J. Toops, A. K. Datye, Z. Li and E. A. Kyriakidou, *ACS Appl. Nano Mater.*, 2023, **6**, 4544–4553.
27 S. Damyanova, B. Pawelec, K. Arishtirova, M. V. M. Huerta and J. L. G. Fierro, *Appl. Catal., B*, 2009, **89**, 149–159.
28 R. K. Singha, A. Shukla, A. Yadav, L. N. Sivakumar Konathala and R. Bal, *Appl. Catal., B*, 2017, **202**, 473–488.
29 M. Li and A. C. van Veen, *Appl. Catal., B*, 2018, **237**, 641–648.
30 Y. Zhang, L. Xu, B. Liu, X. Wang, T. Wang, X. Xiao, S. Wang and W. Huang, *ACS Catal.*, 2023, **13**, 5938–5948.
31 S. S. Kalanur and H. Seo, *J. Energy Chem.*, 2022, **68**, 612–623.
32 M. A. Gaikwad, U. P. Suryawanshi, U. V. Ghorpade, J. S. Jang, M. P. Suryawanshi and J. H. Kim, *Small*, 2022, **18**, 2105084.
33 X. Ding, R. Jiang, J. Wu, M. Xing, Z. Qiao, X. Zeng, S. Wang and D. Cao, *Adv. Funct. Mater.*, 2023, 2306786.
34 Y. Li, M. Je, J. Kim, C. Xia, S. H. Roh, W. So, H. Lee, D.-H. Kim, S. M. Cho, J. W. Bae, H. Choi and J. K. Kim, *Chem. Eng. J.*, 2022, **438**, 135532.
35 S. Kim, S. Ji, K. H. Kim, S. H. Roh, Y. Cho, C.-L. Lee, K.-S. Lee, D.-G. Choi, H. Choi, J. K. Kim and J. H. Park, *Chem. Eng. J.*, 2021, **407**, 126929.
36 Z. Zhang and J. T. Yates, *Chem. Rev.*, 2012, **112**, 5520–5551.
37 S. Krukowski, P. Kempisty and P. Strąk, *J. Appl. Phys.*, 2013, **114**, 063507.
38 C. Jiang, S. J. A. Moniz, A. Wang, T. Zhang and J. Tang, *Chem. Soc. Rev.*, 2017, **46**, 4645–4660.
39 Th. Wolkenstein, in *Advances in Catalysis*, Elsevier, 1960, vol. 12, pp. 189–264.
40 A. Rothschild, Y. Komem and N. Ashkenasy, *J. Appl. Phys.*, 2002, **92**, 7090–7097.
41 Y. Cherif, H. Azzi, K. Sridharan, S. Ji, H. Choi, M. G. Allan, S. Benaissa, K. Saidi-Bendahou, L. Damptey, C. S. Ribeiro, S. Krishnamurthy, S. Nagarajan, M. M. Maroto-Valer, M. F. Kuehnel and S. Pitchaimuthu, *ACS Omega*, 2023, **8**, 1249–1261.
42 J. K. Nørskov, J. Rossmeisl, A. Logadottir, L. Lindqvist, J. R. Kitchin, T. Bligaard and H. Jónsson, *J. Phys. Chem. B*, 2004, **108**, 17886–17892.
43 H. Ren, Y. H. Lee, E. A. Wu, H. Chung, Y. S. Meng, E. E. Fullerton and N. Q. Minh, *ACS Appl. Energy Mater.*, 2020, **3**, 8135–8142.
44 A. Yee, S. J. Morrison and H. Idriss, *J. Catal.*, 1999, **186**, 279–295.
45 M. M. Chirila, K. Sarkisian, M. E. Andrew, C.-W. Kwon, R. J. Rando and M. Harper, *Ann. Occup. Hyg.*, 2015, **59**, 336–346.
46 E. Celik, Y. Ma, T. Brezesinski and M. T. Elm, *Phys. Chem. Chem. Phys.*, 2021, **23**, 10706–10735.
47 W. J. Albery and P. N. Bartlett, *J. Electrochem. Soc.*, 1984, **131**, 315.
48 T. Ioannides and X. E. Verykios, *J. Catal.*, 1996, **161**, 560–569.
49 P. Schlexer, D. Widmann, R. J. Behm and G. Pacchioni, *ACS Catal.*, 2018, **8**, 6513–6525.

50 P. Pantu and G. R. Gavalas, *Appl. Catal., A*, 2002, **223**, 253–260.
51 R. Kumar Singha, A. Shukla, A. Yadav, S. Sain, C. Pendem, L. N. S. Kumar Konathala and R. Bal, *Mol. Catal.*, 2017, **432**, 131–143.
52 M. Danielis, S. Colussi, C. de Leitenburg, L. Soler, J. Llorca and A. Trovarelli, *Catal. Sci. Technol.*, 2019, **9**, 4232–4238.
53 N. I. Santha, M. T. Sebastian, P. Mohanan, N. McN. Alford, K. Sarma, R. C. Pullar, S. Kamba, A. Pashkin, P. Samukhina and J. Petzelt, *J. Am. Ceram. Soc.*, 2004, **87**, 1233–1237.
54 D. Sharma and B. R. Mehta, *J. Alloys Compd.*, 2018, **749**, 329–335.
55 P. Atkins, J. De Paula and J. Keeler, *Atkins' Physical Chemistry*, Oxford University Press, 11th edn, 2017.
56 J. Resasco, L. DeRita, S. Dai, J. P. Chada, M. Xu, X. Yan, J. Finzel, S. Hanukovich, A. S. Hoffman, G. W. Graham, S. R. Bare, X. Pan and P. Christopher, *J. Am. Chem. Soc.*, 2020, **142**, 169–184.
57 S. Xie, L. Liu, Y. Lu, C. Wang, S. Cao, W. Diao, J. Deng, W. Tan, L. Ma, S. N. Ehrlich, Y. Li, Y. Zhang, K. Ye, H. Xin, M. Flytzani-Stephanopoulos and F. Liu, *J. Am. Chem. Soc.*, 2022, **144**, 21255–21266.
58 G. D. J. Smit, S. Rogge and T. M. Klapwijk, *Appl. Phys. Lett.*, 2002, **81**, 3852–3854.
59 N. J. Divins, A. Braga, X. Vendrell, I. Serrano, X. Garcia, L. Soler, I. Lucentini, M. Danielis, A. Mussio, S. Colussi, I. J. Villar-Garcia, C. Escudero, A. Trovarelli and J. Llorca, *Nat. Commun.*, 2022, **13**, 5080.
60 A. Mussio, M. Danielis, N. J. Divins, J. Llorca, S. Colussi and A. Trovarelli, *ACS Appl. Mater. Interfaces*, 2021, **13**, 31614–31623.
61 A. M. Ismail, E. Csapó and C. Janáky, *Electrochim. Acta*, 2019, **313**, 171–178.
62 D. G. Araiza, D. G. Arcos, A. Gómez-Cortés and G. Díaz, *Catal. Today*, 2021, **360**, 46–54.
63 S. Roy, S. Hariharan and A. K. Tiwari, *J. Phys. Chem. C*, 2018, **122**, 10857–10870.
64 L. Yang, L. Li, P. Xia, H. Li, J. Yang, X. Li, X. Zeng, X. Zhang, C. Xiao and Y. Xie, *Chem. Commun.*, 2021, **57**, 11629–11632.
65 S. Lu, B. Weng, A. Chen, X. Li, H. Huang, X. Sun, W. Feng, Y. Lei, Q. Qian and M.-Q. Yang, *ACS Appl. Mater. Interfaces*, 2021, **13**, 13044–13054.
66 S. Yoon, H. Ha, J. Kim, E. Nam, M. Yoo, B. Jeong, H. Y. Kim and K. An, *J. Mater. Chem. A*, 2021, **9**, 26381–26390.
67 J.-X. Liu, Y. Su, I. A. W. Filot and E. J. M. Hensen, *J. Am. Chem. Soc.*, 2018, **140**, 4580–4587.
68 X. Zhang, L. Zhu, Q. Hou, J. Guan, Y. Lu, T. W. Keal, J. Buckeridge, C. R. A. Catlow and A. A. Sokol, *Chem. Mater.*, 2023, **35**, 207–227.
69 Y. Jiang, J. B. Adams, M. van Schilfgaarde, R. Sharma and P. A. Crozier, *Appl. Phys. Lett.*, 2005, **87**, 141917.